ACS OMEGA

http://pubs.acs.org/journal/acsodf

Article

Laser Ablation Nanoarchitectonics of Au–Cu Alloys Deposited on TiO_2 Photocatalyst Films for Switchable Hydrogen Evolution from Formic Acid Dehydrogenation

Dachao Hong,* Aditya Sharma, Dianping Jiang, Elena Stellino, Tomohiro Ishiyama, Paolo Postorino, Ernesto Placidi, Yoshihiro Kon, and Kenji Koga*

Cite This: *ACS Omega* 2022, 7, 31260–31270

Read Online

ACCESS | Metrics & More | Article Recommendations | Supporting Information

ABSTRACT: The regulation of H_2 evolution from formic acid dehydrogenation using recyclable photocatalyst films is an essential approach for on-demand H_2 production. We have successfully generated Au–Cu nanoalloys using a laser ablation method and deposited them on TiO_2 photocatalyst films (Au_xCu_{100-x}/TiO_2). The Au–Cu/TiO_2 films were employed as photocatalysts for H_2 production from formic acid dehydrogenation under light-emitting diode (LED) irradiation (365 nm). The highest H_2 evolution rate for $Au_{20}Cu_{80}/TiO_2$ is archived to 62,500 μmol h^{-1} g^{-1} per photocatalyst weight. The remarkable performance of $Au_{20}Cu_{80}/TiO_2$ may account for the formation of Au-rich surfaces and the effect of Au alloying that enables Cu to sustain the metallic form on its surface. The metallic Au–Cu surface on TiO_2 is vital to supply the photoexcited electrons of TiO_2 to its surface for H_2 evolution. The rate-determining step (RDS) is identified as the reaction of a surface-active species with protons. The results establish a practical preparation of metal alloy deposited on photocatalyst films using laser ablation to develop efficient photocatalysts.

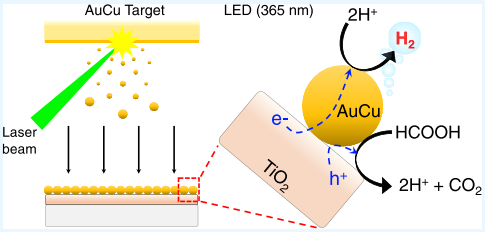

INTRODUCTION

With increasing global energy demand and environmental pressure, H_2 has drawn significant attention in replacing fossil fuels because of its sustainability and environmental friendliness.[1−7] The widespread use of H_2 has practical limitations in several aspects, such as safe storage and transportation. The liquefaction of gaseous H_2 requires high pressure (up to 700 bar) and extremely low temperature (−253 °C), which increases the costs and risks of H_2 storage.[8,9] Chemical compounds such as formic acid containing hydrogen atoms provide an indirect method to store H_2 with potentially low risk and cost. Formic acid dehydrogenation (HCOOH → CO_2 + H_2) can produce gaseous H_2 in the presence of a catalyst.[10,11] Noble metal (e.g., Pt, Pd, and Ir) nanoparticles (NPs) are generally used as catalysts for H_2 production from formic acid dehydrogenation.[12−14] However, formic acid dehydrogenation based on the thermal catalytic reactions may not be terminated until formic acid is completely consumed. Therefore, to regulate H_2 evolution from formic acid dehydrogenation, an on/off switch by light would be an essential tool for on-demand H_2 production.

Several reports show that photocatalysts with noble metal-based NPs in a suspended powder form can produce H_2 from formic acid dehydrogenation.[15−24] Among them, noble metal NPs deposited on TiO_2-based photocatalysts have gained widespread attention with good photostability, activity, nontoxicity, and low cost for practical applications.[25] Typically, metal NP-deposited TiO_2 photocatalysts are utilized as suspended powders in the reaction. Thus, it could face difficulties in separating and recovering the photocatalyst NPs without any loss from reaction solutions. Additionally, the conjunction of metal NPs onto TiO_2 generally comprises several complex and multiple reaction steps to obtain nanoscale materials with homogeneous chemical compositions and sizes. In a conventional method, tailoring the form and composition of the nanomaterials requires several parameters such as morphological tuners, toxic reagents, and organic solvents. Organic or inorganic residues in photocatalysts derived from chemical reagents and organic solvents could deactivate and reduce catalytic performance.[26]

Conversely, as a physical method, the laser ablation technique is regarded as a new green technology because of its versatility and simplicity. Recently, it has been demonstrated that the fabrication of alloy NPs through laser ablation affords unique physical and chemical properties beneficial for catalytic applications.[27,28] The laser ablation of alloy targets in inert gases (e.g., He and Ar) can quickly generate nanoalloys with various compositions by changing source-target compo-

Received: June 5, 2022
Accepted: August 4, 2022
Published: August 22, 2022

sitions without using complex chemical routes.[29,30] This physical method has additional merit for avoiding surfactants, capping agents, or metal ions, which are considered to decrease catalytic performance. Au can be a promising candidate cocatalyst for switchable photocatalytic H_2 evolution from formic acid dehydrogenation because Au NPs are thermally inactive for H_2 evolution from formic acid dehydrogenation at ambient temperature.[31] Alloy NPs composed of Au and other metals can reduce Au usage and potentially enhance the catalytic performance by the alloy effect.[32−34] In addition, Cu is an abundant metal and can form a homogeneous AuCu alloy, which is suitable for a model case by the laser ablation synthesis. Furthermore, the activity and role of Au and Cu metals have not yet been investigated and understood in the photocatalytic H_2 evolution from formic acid dehydrogenation.

In this work, we successfully prepared well-defined Au−Cu NPs in the gas phase using a laser ablation method and deposited them onto TiO_2 NP films (Au_xCu_{100-x}/TiO_2, x = 0−100 at%). The NPs were prepared without contaminants, surfactants, or toxic reagents to obtain homogeneous Au−Cu alloys on TiO_2 photocatalyst films. The as-prepared Au_xCu_{100-x}/TiO_2 films were evaluated for the photocatalytic H_2 evolution from formic acid dehydrogenation. The Au-Cu/TiO_2 photocatalyst film exhibited significantly high H_2 production under LED irradiation, demonstrating the advantage of the laser ablation method for NP synthesis. No H_2 evolution in the dark proves useful for the light-switchable H_2 evolution from formic acid dehydrogenation. The $Au_{20}Cu_{80}/TiO_2$ film achieved a H_2 evolution rate per photocatalyst weight of 62,500 μmol h^{-1} g^{-1} owing to the formation of a Au-rich surface on $Au_{20}Cu_{80}$ NPs during the photocatalytic reactions. This is the first work that shows efficient H_2 evolution from formic acid dehydrogenation using Au−Cu/TiO_2 photocatalyst films prepared by the laser ablation. The mechanism insight into the photocatalytic H_2 evolution by Au−Cu/TiO_2 was investigated based on X-ray photoelectron spectroscopy (XPS), X-ray diffraction (XRD), and electrochemical impedance spectroscopy (EIS). The results clarify that Au accelerates the electron migration in the reaction, and the rate-determining step (RDS) is involved in the reaction of the surface-active species with protons.

EXPERIMENTAL SECTION

Chemicals. Au_xCu_{100-x} alloy targets (x = 0, 5, 10, 20, 40, 50, 60, 80, and 100 at%) for the laser ablation were obtained from Rare Metallic Co., Ltd. (Japan). Titanium dioxide P25 (TiO_2 P25) was purchased from EVONIK (Germany). Nitric acid (HNO_3), ethanol, and formic acid were purchased from Wako Pure Chemicals (Japan). All reagents were used without further purification. Purified water (18.2 MΩ cm) was obtained from a Milli-Q system (Direct-Q3 UV, Millipore).

Characterization Methods. The morphology of the photocatalysts was observed using a JEOL JEM-2010 transmission electron microscope with an accelerating voltage of 200 kV. The mean particle size of each sample was calculated by counting 200 particles from the transmission electron microscopy (TEM) image using ImageJ software. The lattice parameters and chemical compositions of the prepared Au−Cu nanoalloys were examined by X-ray diffraction (XRD) in the thin film mode at θ = 0.3°. The X-ray source was operated at 40 kV and 200 mA with Cu Kα radiation of 0.154178 nm. The X-ray photoelectron and X-ray-induced Auger spectra were recorded on catalyst films using a KRATOS ULTRA2 X-ray photoelectron spectroscopy (XPS) system with an Al Kα monochromatic X-ray source (1486.6 eV) and with a SPECS PHOIBOS 150 XPS system equipped with an Al Kα monochromatic X-ray source (XR50 MF). The binding energy (BE) was calibrated by the Ti $2p_{3/2}$ peak (458.8 eV) as an internal standard.[35] Inductively coupled plasma mass spectrometry (ICP-MS) was carried out to analyze the chemical composition of the Au−Cu NPs. The UV−vis diffuse reflectance spectroscopy (DRS) spectra were recorded on a V-770 spectrophotometer (JASCO, Japan). The Raman spectra were collected on $Au_{20}Cu_{80}/TiO_2$ films before and after a 1 h immersion in a formic acid solution (0.010 M). After the treatment, the samples were rinsed with water and dried *in vacuo*. Measurements were carried out using a He−Ne laser (λ = 632.8 nm) coupled with a 600 lines mm^{-1} grating monochromator and a charge-coupled device (CCD). Incident radiation was focused on the sample using a 10× objective, and thereafter, the peak was collected in a back-scattering configuration.

Synthesis of TiO_2 Films. To prepare the TiO_2 films, TiO_2 P25 (10 g) was suspended in ethanol (10 mL) with a drop of HNO_3 (0.10 M, 10 μL) and ultrasonicated for 20 min to form 1.0 g mL^{-1} P25 colloidal suspension (1.0 g L^{-1}). It was deposited onto a quartz glass plate (20 mm × 20 mm) by spin-coating (2000 rpm for 45 min) with a drop rate of 33 μL min^{-1}, and the P25-coated plate was calcined at 500 °C for 5 h in O_2 flow to obtain the TiO_2 particulate film.

Preparation of Au−Cu/TiO_2 Photocatalyst Films. The schematic diagram of the apparatus is illustrated in Figure 1.

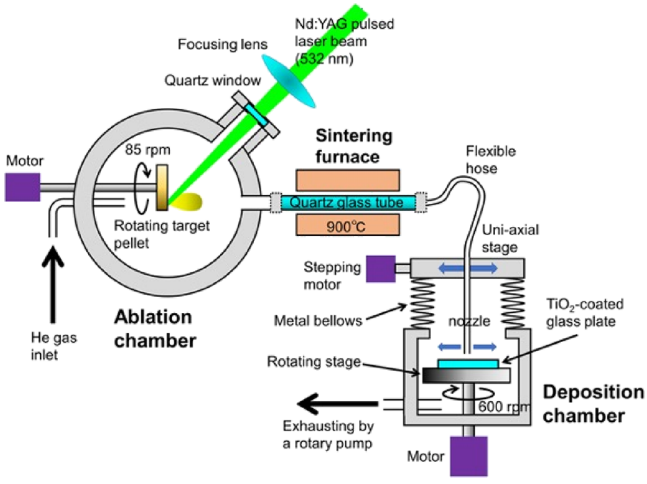

Figure 1. Schematic illustration of the Au−Cu alloy deposition on TiO_2 films by the laser-deposition technique.

Briefly, the system consisted of three parts: a laser ablation chamber, a sintering furnace, and a deposition chamber. A target pellet (19 mm in diameter, 4 mm thick) rotating at 85 rpm was irradiated (3.0 mm ϕ spot size) by the second harmonic (532 nm, 40 or 50 mJ/pulse, 5.0 Hz) of an Nd:YAG laser (Surelite SLI-20, Continuum) at a pulse width of 4−6 ns. The sample pictures are shown in Figure S1. The weight of each photocatalyst (~0.42 mg) was determined by subtracting the weight of the quartz glass from the total weight.

Evaluation of H_2 Evolution. The setup for H_2 evolution from formic acid dehydrogenation is shown in Figure S2. In a typical experiment, a vial (70 mL) containing a Au−Cu/TiO_2 film (19 mm × 19 mm) immersed in formic acid (0.010 M, 30

https://doi.org/10.1021/acsomega.2c03509
ACS Omega 2022, 7, 31260−31270

mL) was sealed using a rubber septum and Teflon tape. The reactor was deaerated before the reaction by purging Ar for 30 min. The formic acid solution was stirred continuously to ensure homogeneous distribution and reaction with the photocatalyst film. Thereafter, the vial was irradiated using an LED lamp (λ = 365 nm) to initiate H_2 evolution from formic acid dehydrogenation. The intensity of the light irradiated on the photocatalyst films was adjusted to be 4.3−30 mW cm^{-2}. After every 60 min of the irradiation, the gas evolved in the headspace (40 mL) of the reaction vial was sampled using a gastight syringe (100 μL) and quantified using a Shimadzu GC-2014 gas chromatograph (Ar carrier gas, Shincarbon-ST column) equipped with a thermal conductivity detector.

Calculation of the Apparent Quantum Yield (AQY). The AQY for H_2 evolution was calculated according to the previous literature.[36,37] The AQY of the modified samples under LED irradiation (365 nm) was determined by the following equation.

$$\mathrm{AQY} = \frac{\text{number of reacted electrons}}{\text{number of incident photons}} \times 100 = \frac{2N_{H_2}N_A hc}{PS\lambda t} \times 100$$

where N_{H_2} (moles) is the amount of hydrogen evolved, N_A is Avogadro's constant (6.02×10^{23} mol^{-1}), h is Planck's constant (6.62×10^{-34} J s^{-1}), c is the speed of light (3.08×10^{8} m s^{-1}), and P indicates the power of light intensity (8.0×10^{-3} W cm^{-2}) on an irradiation area S (4.0 cm^2) with a wavelength (λ) of 3.65×10^{-7} nm for a duration (t) of 3600 s.

Electrochemical Impedance Spectroscopy (EIS) Measurements. The EIS measurements were performed in a standard three-electrode system in formic acid solution (0.010 M). The silver/silver chloride (Ag/AgCl) and Pt wire were used as reference and counter electrodes, respectively. The Au−Cu alloy NPs deposited on TiO_2-coated ITO films (15 mm × 19 mm) were used as the working electrode. The formic acid solution was purged with Ar for 30 min prior to the measurement. The light intensity of the light irradiated on the photocatalyst films was adjusted to be 15 mW cm^{-2}. The impedance spectra were measured in potentio-electrochemical impedance spectroscopy mode over the frequency range of 1.0 MHz to 0.10 Hz with an amplitude of 20 mV using the potentiostat (SP-200, Bio-Logic Inst.). The obtained spectra were fitted with an equivalent circuit model.

RESULTS AND DISCUSSION

Synthesis and Characterization of Au−Cu/TiO_2 Photocatalysts. The schematic representation of the Au−Cu/TiO_2 film fabrication process is illustrated in Figure 1. The Au−Cu/TiO_2 films were synthesized as follows: First, the TiO_2 film was obtained by immobilizing TiO_2 nanoparticles on a quartz wafer by a spin coating method followed by calcination. Thereafter, the deposition of the Au−Cu alloy NPs on the TiO_2 films was performed via a laser ablation method with Au−Cu source targets along with an aerosol deposition technique. Tiny aggregates created in the ablation chamber were sintered to spherical NPs when transported through a quartz tube heated using a furnace at 900 °C. The NPs were further transported with the He stream into the deposition chamber, in which they were deposited on the TiO_2 film-coated quartz substrate. We successfully prepared a homogeneous deposition over the entire film area by uniaxially scanning the blowout nozzle facing the rotating sample surface at speed proportional to the reciprocal distance from the rotation center. The Au−Cu NPs deposited on the TiO_2 films are denoted as Au_xCu_{100-x}/TiO_2 (x = 0, 5, 10, 20, 40, 50, 60, 80, and 100 at%) photocatalyst films (Figure S1). No additional pretreatments, such as washing and calcination, were required for the as-prepared samples by the laser ablation method compared to those prepared by sol−gel solution methods.[38−40] The as-prepared Au−Cu/TiO_2 films were characterized by powder XRD, TEM, UV−vis DRS, and XPS analyses to examine the structure and composition.

The crystal structure of the as-prepared Au−Cu/TiO_2 films was characterized by powder XRD. Figure 2 shows the XRD patterns of TiO_2 and Au−Cu/TiO_2 films with different Au contents. The pure TiO_2 film showed diffraction peaks from anatase-type TiO_2 centered at 36.9°, 37.8°, 38.6°, 48.0°, 53.9°, and 55.1° and from rutile-type TiO_2 centered at 36.1°, 39.2°, 41.2°, 44.0°, 54.3°, and 56.6°. Au−Cu/TiO_2 showed the 111 and 200 peaks of the Au−Cu NPs, and their positions shifted to relatively high angles with the decrease in Au content. The compositions of Au−Cu were calculated based on Vegard's law[33,41] and were in good accordance with the corresponding Au−Cu alloy targets and ICP-MS analysis results (Table S1).

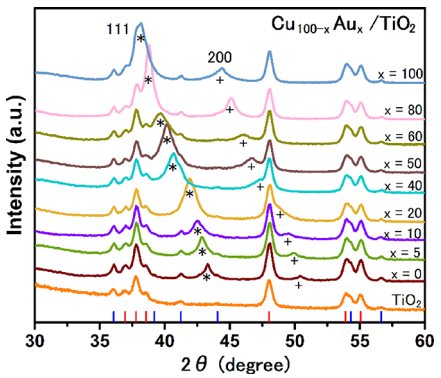

Figure 2. XRD patterns of the prepared TiO_2 and Au_xCu_{100-x}/TiO_2 (x = 0−100 at%) films. The red and blue bars at the bottom denote the diffraction peaks from anatase and rutile phases of TiO_2, respectively. The markers of * and + correspond to the 111 and 200 peaks from Au−Cu NPs, respectively.

The nanoscale morphologies of the Au−Cu/TiO_2 films were explored by TEM measurements (Figure 3 and Figure S3). The $Au_{20}Cu_{80}$ spherical alloy NPs were well dispersed on the TiO_2 film with an average particle size of 13.3 nm. All the Au−Cu/TiO_2 NPs were distributed on the TiO_2 films with similar

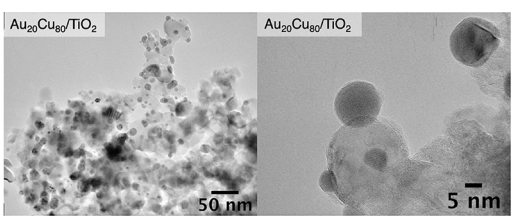

Figure 3. TEM images of the $Au_{20}Cu_{80}/TiO_2$ NPs with corresponding high-magnification images. See Figure S3 for the other TEM images of the Au−Cu/TiO_2 NPs.

https://doi.org/10.1021/acsomega.2c03509
ACS Omega 2022, 7, 31260−31270

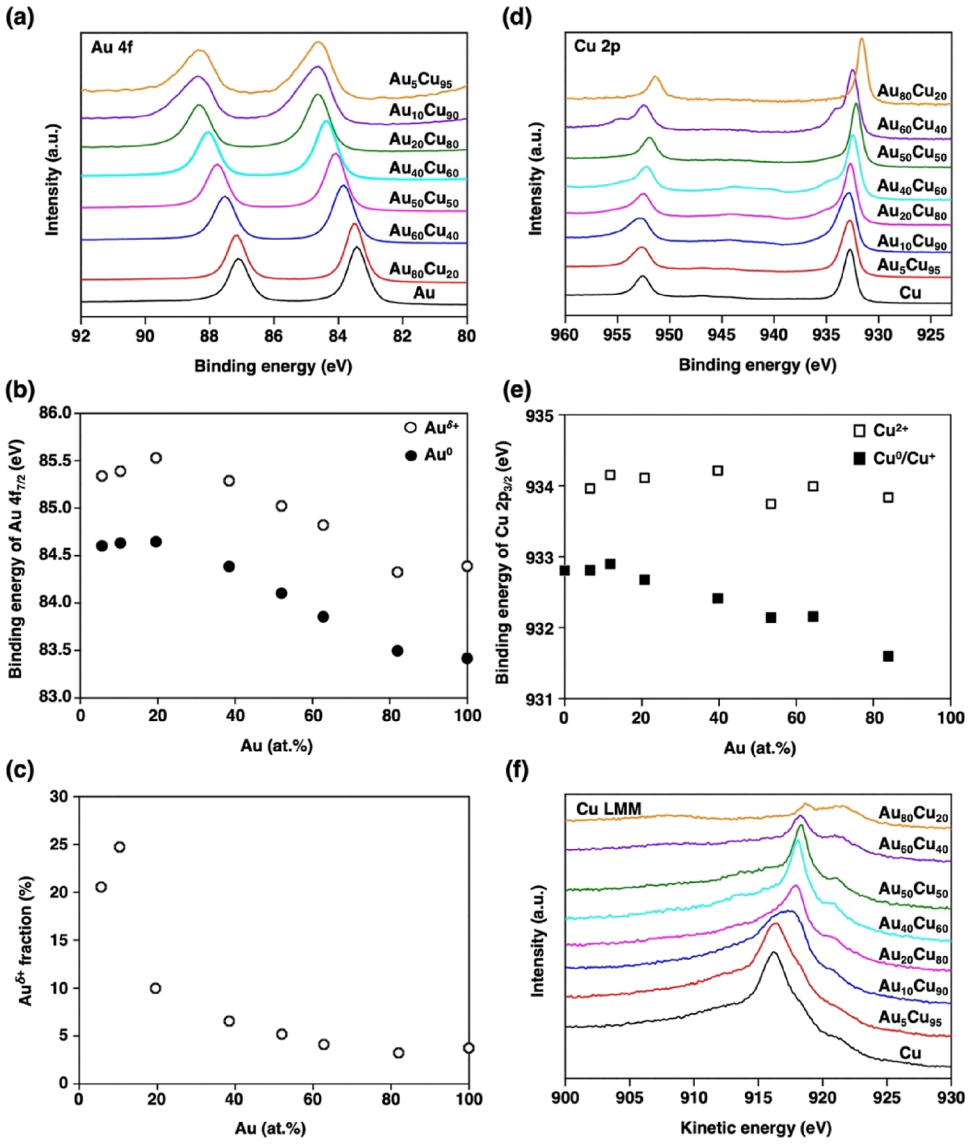

Figure 4. (a) XPS spectra of Au 4f, (b) deconvoluted Au^0 and $Au^{\delta+}$ peak values plotted against Au content, (c) relative $Au^{\delta+}$ fraction plotted against Au content, (d) XPS spectra of Cu 2p, (e) Cu $2p_{3/2}$ (Cu^{2+} and Cu^0/Cu^+) binding energy plotted against Au content, and (f) Cu LMM spectra obtained from the Au−Cu/TiO_2 films; the deconvoluted Au 4f and Cu 2p peaks are shown in Figure S7.

particle sizes within 10−30 nm (Figure S4). The diffuse reflectance UV−vis spectra of Au−Cu/TiO_2 films are shown in Figure S5. Broad absorption bands at approximately 530 nm for Au/TiO_2 and 600 nm for Cu/TiO_2 were attributed to the localized surface plasmon resonance of Au and Cu NPs, respectively. The plasmon peaks of Au−Cu/TiO_2 exhibited a red shift with an increase in Cu content in accordance with the alloy effect of Au and Cu.[42] The results indicate that the laser ablation method for preparing Au−Cu NPs provides easy and precise control of alloy compositions by using the corresponding alloy targets. Since the deposited Au−Cu NPs were uniform in morphology and size, we accurately evaluated and compared the catalytic activity of each photocatalyst film to investigate the catalytic mechanism.

Surface Characterization of Au−Cu/TiO_2 by XPS Spectroscopy. XPS measurements were performed as shown in Figure 4 and Figures S6 and S7 to understand the surface conditions of the Au−Cu/TiO_2 films. The Au $4f_{7/2}$ and $4f_{5/2}$ peaks of the Au/TiO_2 film were centered at 83.4 and 87.1 eV, respectively (Figure 4a). The Au content on the surface of Au−Cu/TiO_2 was calculated from the XPS spectra of the Au $4f_{7/2}$ and Cu $2p_{3/2}$ areas normalized with cross-sectional factors, as shown in Table S1. The surface Au content obtained from the XPS spectra is consistent with those obtained from XRD and ICP−MS analyses. The Au 4f peaks in the Au/TiO_2 film shifted to lower binding energies than pure Au, of which the $4f_{7/2}$ peak is located at 84.0 eV.[35,43] The result suggests that the electrons migrate from TiO_2 to Au because the work function of Au (5.10−5.28 eV) is larger than that of TiO_2 (4.6−4.7 eV).[44] The peaks with a spin−orbit splitting of Δ = 3.67 eV in the Au 4f region showed the presence of metallic Au in the Au/TiO_2 film. As the Cu content increased in Au−Cu/TiO_2, the Au 4f peaks shifted to higher binding energies. This observed shift to high binding energies in the Cu-rich alloys on TiO_2 was attributed to the inherent nature of the alloy itself because of the depletion of Au 5d electrons caused by dilution of Au atoms in Cu atoms.[45,46] We also performed XPS measurements for Au−Cu alloy NPs deposited on conductive carbon papers (Au−Cu/CP) to investigate the electron transfer between the Au−Cu nanoalloys and the TiO_2

https://doi.org/10.1021/acsomega.2c03509
ACS Omega 2022, 7, 31260−31270

semiconductor in Au−Cu/TiO_2 (Figure S6a). The Au $4f_{7/2}$ peak of Au/CP was observed at 84.1 eV, consistent with the standard value,[47] while that of Cu-rich Au−Cu NPs on CP showed nearly the same values as on TiO_2. We thus conclude that the electron transfer between Au−Cu NPs and TiO_2 occurs when the Au content is more than 20 at%.

In addition, we also obtained a $Au^{\delta+}$ component in the Au−Cu/TiO_2 films by analyzing the Au 4f spectra, as shown in Figure 4b (Figure S6b for Au−Cu/CP). The deconvolution peaks assigned to $Au^{\delta+}$ shifted by +0.8 eV from the Au^0 peaks. The $Au^{\delta+}$ fractions calculated from the deconvoluted peak areas rapidly increased at the two Cu-rich alloys (Au_5Cu_{95} and $Au_{10}Cu_{90}$) on TiO_2, as shown in Figure 4c, but did not markedly increase for Au−Cu/CP (Figure S6c). A similar result was reported previously for Au−Pd and Au−Cu alloys deposited on TiO_2,[48] suggesting that the alloying effect of Cu could affect the Au metallic state. This might suggest the easier formation of Au−O bonding for interfacial Au atoms diluted by Cu atoms in Cu-rich alloys.[49]

The Cu 2p peaks of the Au−Cu/TiO_2 films are shown in Figure 4d and deconvoluted to the main component (Cu^0 or Cu^+) and a subcomponent (Cu^{2+}) (Figure S7). No charge transfer between the two Cu-rich alloys (Au_5Cu_{95} and $Au_{10}Cu_{90}$) and TiO_2 was observed because the work function of Cu (4.65 eV)[45] is similar to that of TiO_2 (4.6−4.7 eV). Figure 4e shows that the main component for Au−Cu/TiO_2 shifted to lower binding energy when the Au content is higher than 20 at%, whereas no shift is observed for Au−Cu/CP (Figure S6e). This suggests that the electrons migrate from TiO_2 to Cu atoms through the Au-rich side. The peak shifts in the Au−Cu alloy agree with the previously reported literature.[50−52] The Cu LMM spectra were analyzed to distinguish Cu^0 and Cu^+ (Figure 4f and Figure S6f). The kinetic energies of Cu LMM in Cu/TiO_2 and Au_5Cu_{95}/TiO_2 were centered at 916.2 eV, corresponding to the Cu^+ component.[53] The Cu LMM peaks in Au−Cu/TiO_2 with more than 20 at% Au appeared at 918.6 eV, denoting the presence of Cu^0. Although a Cu LMM peak for the Cu^{2+} component is generally observed between the Cu^+ and Cu^0 LMM peaks, its contribution could be small because of the lower Cu^{2+} fractions. The XPS results indicate that the surface Cu in the Au−Cu alloys had oxidation resistance[54] when the Au content was higher than 20 at%. The Au_5Cu_{95} and $Au_{10}Cu_{90}$ alloy NPs on the TiO_2 films formed a Au−Cu_2O mixed layer in atmospheric conditions.

H_2 Evolution from Formic Acid Dehydrogenation. We employed the well-characterized Au−Cu/TiO_2 films for the photocatalytic H_2 evolution from formic acid dehydrogenation under LED irradiation (λ = 365 nm, 8.0 mW cm^{-2}). First, we examined the activity of pure Au and Cu deposited on the TiO_2 NP films to confirm the efficiency of the light on/off switch for H_2 evolution from formic acid dehydrogenation. The time courses of the H_2 evolution amount by Cu/TiO_2, Au/TiO_2, and Au/TiO_2 without light irradiation are shown in Figure 5. Further, in formic acid dehydrogenation, an equal quantity of CO_2 ($HCOOH \rightarrow CO_2 + H_2$) and small amounts of CO ($HCOOH \rightarrow CO + H_2O$) were also observed (Figure S8). No H_2 evolution was observed from Au/TiO_2 in the dark. The result suggests that the UV light on/off switch can regulate the H_2 evolution from formic acid dehydrogenation using the Au−Cu/TiO_2 photocatalyst films. The H_2 evolution rates were obtained as 1.7 and 9.7 μmol h^{-1} for Cu/TiO_2 and Au/TiO_2, respectively, under the LED irradiation of 8.0 mW cm^{-2}. The H_2 evolution rate per photocatalyst weight for Au/TiO_2 was calculated to be 24,200 μmol h^{-1} g^{-1}, which is a high rate compared to the reported photocatalysts for H_2 evolution from formic acid dehydrogenation (Table S2). The results demonstrate the advantage of the laser ablation method for the surfactant-free synthesis of Au NPs deposited on the TiO_2 NP films, which can be effectively used for on-demand H_2 production from formic acid dehydrogenation.

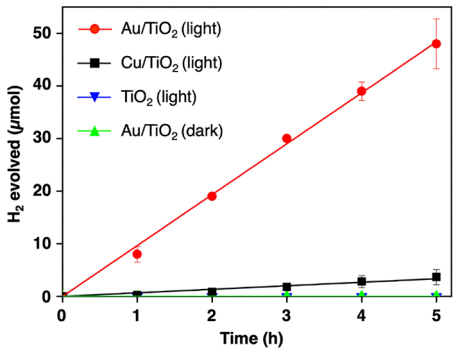

Figure 5. Time courses of H_2 evolution by the irradiation (365 nm, 8.0 mW cm^{-2}) of TiO_2, Cu/TiO_2, and Au/TiO_2 and Au/TiO_2 photocatalysts in the dark in formic acid solutions (0.010 M, 30 mL).

We examined the H_2 evolution of Au−Cu alloy NPs with different compositions deposited on the TiO_2 film. The H_2 evolution rates were plotted against the Au content calculated from XRD measurements as shown in Figure 6a (see Figures S9 and S10 for the time profile of H_2, CO_2, and CO evolution). The H_2 evolution rates were saturated at the Au content of 20%. Notably, the activity of $Au_{20}Cu_{80}$/TiO_2 was comparable with that of Au/TiO_2. The AQY was calculated to be ~6.0% for Au_xCu_{100-x}/TiO_2 ($x \geq 20$ at%) (Figure S11). The results suggest that utilizing base metals as alloying agents can minimize Au usage for practical application. Hence, we used the optimized $Au_{20}Cu_{80}$/TiO_2 photocatalyst for further evaluation.

The H_2 evolution rates of $Au_{20}Cu_{80}$/TiO_2 obtained at different wavelengths were overlaid with the diffuse reflectance UV−vis spectra of $Au_{20}Cu_{80}$/TiO_2 and TiO_2 films (Figure 6b and Figure S12). No discernible H_2 evolution was observed for $Au_{20}Cu_{80}$/TiO_2 at the irradiation of 420, 450, 530, and 590 nm, indicating that the photoexcitation of TiO_2 initiated the photocatalytic H_2 evolution. The plasmonic effect derived from the Au−Cu alloy NPs was not involved in the photocatalytic H_2 evolution. The light intensity dependence of the H_2 evolution rates for $Au_{20}Cu_{80}$/TiO_2 at 365 nm is presented in Figure S13. H_2 evolution was observed with the increase in light intensity from 4.3 to 30 mW cm^{-2}. The result suggests that the photocatalytic H_2 evolution from formic acid dehydrogenation occurs through a one-photon/one-electron process.[36] Moreover, the H_2 evolution rate of $Au_{20}Cu_{80}$/TiO_2 reached 62,500 μmol h^{-1} per photocatalytic weight at the light intensity of 30 mW cm^{-2}, demonstrating the high efficiency of the H_2 evolution with the use of the Au−Cu cocatalyst among the reported photocatalysts (Table S2). The reported photocatalyst NPs dispersed in reaction solutions have higher reaction probability than AuCu/TiO_2 photocatalysts immobilized in quartz plates for the activity comparison.

Nevertheless, the superior performance of the AuCu/TiO_2 photocatalyst films may account for the uniform deposition of AuCu alloy on TiO_2 films and free surfactants and ion residues on the AuCu surface. The uniform deposition of AuCu alloy

https://doi.org/10.1021/acsomega.2c03509
ACS Omega 2022, 7, 31260−31270

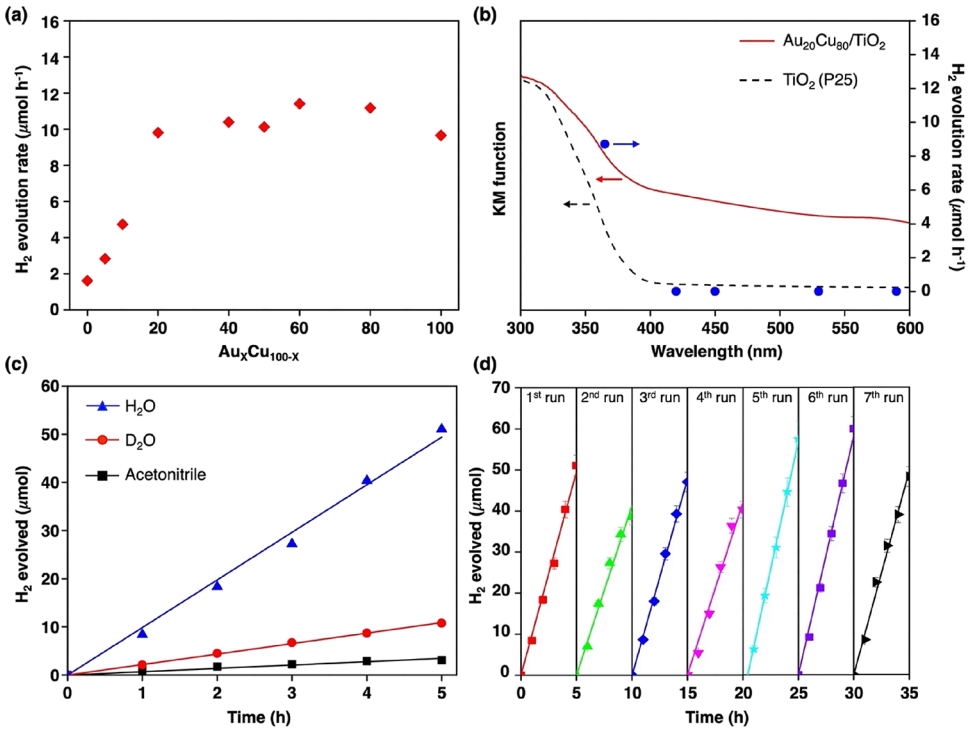

Figure 6. (a) H_2 evolution rates of Au_xCu_{100-x}/TiO_2 (x = 0−100) photocatalysts plotted against the Au content calculated from XRD measurements. (b) Wavelength dependence of the H_2 evolution rates of $Au_{20}Cu_{80}TiO_2$ (λ = 365, 420, 450, 530, and 590 nm). (c) Time courses of H_2 evolution under the irradiation (365 nm, 8.0 mW cm^{-2}) of the $Au_{20}Cu_{80}TiO_2$ photocatalyst film in H_2O, D_2O, and acetonitrile containing formic acid (0.010 M). (d) Repetitive photocatalytic H_2 evolution from formic acid dehydrogenation over $Au_{20}Cu_{80}/TiO_2$ under LED irradiation (365 nm, 8.0 mW cm^{-2}) in formic acid solution.

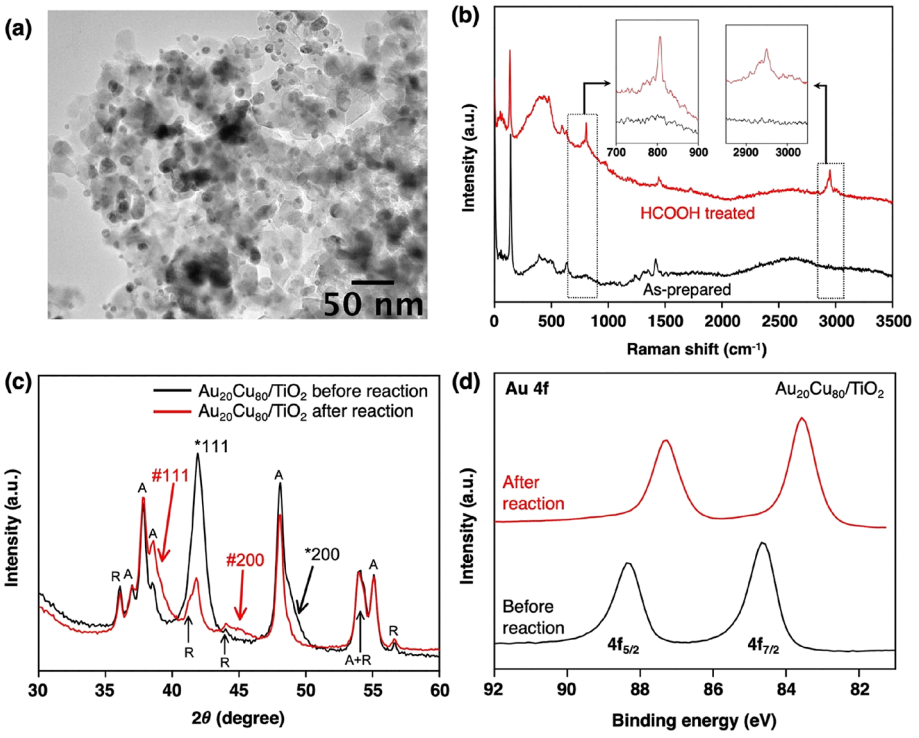

Figure 7. Characterizations of the $Au_{20}Cu_{80}/TiO_2$ film before and after the H_2 evolution from formic acid dehydrogenation. (a) TEM image after reaction, (b) Raman spectra before and after treatment of formic acid, (c) XRD spectra, and (d) XPS spectra.

NPs on TiO_2 films by laser ablation will show a more effective surface area of AuCu NPs exposed to the reaction solution working as active sites toward H_2 evolution. Compared to laser ablation deposition, metal NP-loaded TiO_2 photocatalysts prepared by sol−gel solution methods may reduce their effective surface area because parts of their metal NPs may be

https://doi.org/10.1021/acsomega.2c03509
ACS Omega 2022, 7, 31260−31270

embedded and surrounded by TiO_2. Additionally, organic and inorganic residues on metal surfaces may decrease catalytic activity. Although AgPd@Pd/TiO_2 NPs in powder form showed an excellent H_2 evolution rate under the irradiation of a Xe lamp,[24] it was not suited for the light-switchable H_2 evolution because the H_2 evolution was observed even without light irradiation. CdS/CoP@rGO NPs in powder form were also reported to exhibit a high H_2 evolution rate under LED irradiation with a low light intensity.[55]

The H_2 evolution of the $Au_{20}Cu_{80}TiO_2$ film was also performed in acetonitrile (MeCN) and deuterium water (D_2O) as shown in Figure 6c. The low H_2 evolution rate in MeCN (0.7 μmol h^{-1}) indicates that H_2O acts as a proton source in the H_2 evolution reaction. The kinetic isotope effect (KIE) on H_2 evolution using D_2O was determined in formic acid dehydrogenation. The H_2 evolution rate in D_2O was obtained to be 2.2 μmol h^{-1} with the corresponding KIE value of 4.5 (KIE = [H_2 evolution rate in H_2O]/[H_2 evolution rate in D_2O]). The large KIE value indicates that the RDS of the H_2 evolution is involved in the reaction of surface-active species on Au−Cu alloy with H_2O (protons).[6]

The recycling and reusability of photocatalysts are crucial factors in practical application. We carried out repeated experiments to examine the stability of the $Au_{20}Cu_{80}/TiO_2$ photocatalyst. After each reaction, the $Au_{20}Cu_{80}/TiO_2$ film was rinsed with water and dried *in vacuo*; afterward, it was reused for the repeated reaction with a freshly prepared formic acid solution. The high photocatalytic performance was maintained even after seven cycles (Figure 6d). The maintained activity suggests that the evolved CO does not deactivate the $Au_{20}Cu_{80}$ surface in the reactions. For H_2 evolution from formic acid dehydrogenation, metal NP catalysts are commonly used as suspended solutions.[56−58] Generally, it is difficult to separate photocatalyst NPs from reaction solutions for further use and recover all photocatalysts without weight loss during the recycling process. Our $Au_{20}Cu_{80}/TiO_2$ immobilized on quartz plates showed superior photocatalyst recovery. We also performed an extended duration test for $Au_{20}Cu_{80}/TiO_2$ in the H_2 evolution (Figure S14). The H_2 evolution linearly increased until 28 h, reaching 131.4 μmol. The evolved H_2 was saturated after 28 h because of formic acid consumption. The results demonstrate the high recyclability and durability of the $Au_{20}Cu_{80}/TiO_2$ film in the H_2 production from formic acid dehydrogenation.

Characterizations of $Au_{20}Cu_{80}/TiO_2$ after the Reactions. After the reaction, the $Au_{20}Cu_{80}/TiO_2$ photocatalyst plate was washed with water, dried *in vacuo*, and characterized using TEM, Raman scattering, and XRD and XPS spectroscopies. Figure 7a displays the TEM images of the $Au_{20}Cu_{80}/TiO_2$ NPs after the reaction. The morphology and particle size distribution did not significantly change even after seven consecutive runs (Figure S15). The Raman spectra were obtained from the as-prepared $Au_{20}Cu_{80}/TiO_2$ and immersed in formic acid for 1 h (Figure 7b). The characteristic Raman peaks that appeared at 800 and 2950 cm^{-1} can be assigned to the vibrational modes of HCOO molecules.[59] The characteristic peaks disappeared after light irradiation onto the formic acid-treated $Cu_{80}Au_{20}/TiO_2$. The results demonstrated that formic acid was first adsorbed on the photocatalyst surface and then dehydrogenated to H_2 and CO_2 during LED irradiation. As shown in Figure 7c, the XRD peaks of the original Au−Cu phase (denoted as *111 and *200) in $Au_{20}Cu_{80}/TiO_2$ decreased after the reaction, while the new peaks at around 38.6° and 45.0° grew, which correspond to Au-rich Au−Cu phases (denoted as #111 and #200). The results indicate that a portion of Cu atoms leached from the original alloy NPs. Additionally, the XPS spectrum of $Au_{20}Cu_{80}/TiO_2$ for Au $4f_{7/2}$ was significantly shifted from 84.6 to 83.6 eV after the reaction (Figure 7d), suggesting that the Au−Cu alloy surfaces became Au-rich. The surface Au compositions of $Au_{20}Cu_{80}/TiO_2$ were increased from 20.8 to 34.7 at% after the reaction (Figure S16), which were estimated from the XPS spectra of the Au $4f_{7/2}$ and Cu $2p_{3/2}$ areas normalized with cross-sectional factors. The XPS result indicates that the outermost surface of $Au_{20}Cu_{80}$ after the reaction can form a Au-rich surface since the 34.7 at% Au content obtained from XPS data is the average value obtained probing a 1−2 nm layer. Both XRD and XPS measurements confirmed the partial Cu leaching from $Au_{20}Cu_{80}/TiO_2$ after the reaction. Further, the Cu 2p and Cu LMM spectra of $Au_{20}Cu_{80}/TiO_2$ after the reaction are depicted in Figure S17. The Cu LMM pattern showed that the surface Cu atoms were maintained in a metallic Cu^0 state similar to that before the reaction. The metallic Au−Cu surfaces contributed to the high H_2 evolution obtained from the $Au_{20}Cu_{80}/TiO_2$ photocatalyst.

The H_2 evolution was sharply decreased when the Au content was lower than 20 at% (Figure 6a). To understand the reactivity difference, we analyzed the relative Cu content on the surfaces from the XPS spectra of the Au $4f_{7/2}$ and Cu $2p_{3/2}$ areas before and after the reaction (Figure S16). After the reaction, the Cu content in the Au_5Cu_{95}/TiO_2 and $Au_{10}Cu_{90}/TiO_2$ photocatalysts significantly decreased from 95.7 and 87.9 at% to 35.0 and 42.6 at%, respectively. The result suggests that the Cu atoms on the alloys were oxidized to Cu^+ and thus leached into the acidic solutions during the photocatalytic reactions. Before the reaction, the oxidized Cu layers (Cu_2O) on the surfaces of Au_5Cu_{95}/TiO_2 and $Au_{10}Cu_{90}/TiO_2$ were also characterized by the Cu Auger spectra (Figure 4f). The formed Cu_2O layer or Cu^+ may inhibit the formation of an active species on the surface for subsequent H_2 evolution, resulting in low activity. Although less Cu leaching was observed on the surface of $Au_{20}Cu_{80}/TiO_2$ after the reaction, the surface Cu atoms were also maintained in a metallic state after the reaction (Figure S17). Thus, one of the reasons for the reactivity difference between $Au_{20}Cu_{80}/TiO_2$ and $Au_{10}Cu_{90}/TiO_2$ can be the deterioration of the oxidation resistance on Au−Cu surfaces.

Mechanistic Insight into the H_2 Evolution. The EIS measurement was carried out under the LED irradiation of Au−Cu/TiO_2 films in the formic acid solution (0.010 M) to determine the electron transfer efficiency (Figure 8). The EIS Nyquist plots in the spectra can be assigned to the solution resistance (R_{sol}), the electrochemical electron transfer resistance (R_{et}), and the reaction resistance of formic acid decomposition (R_{re}) in descending order from the high-frequency side. The resistance values obtained by fitting the plots with an equivalent circuit model are summarized in Table S3 and Figure S18. As shown in Figure 8, Au/TiO_2 displayed the smallest radius, followed by $Au_{50}Cu_{50}/TiO_2$, $Au_{20}Cu_{80}/TiO_2$, $Au_{10}Cu_{90}/TiO_2$, and Au_5Cu_{95}/TiO_2. The smaller radius in the EIS Nyquist plot indicates a lower R_{et} of the electrodes. On the contrary, the relatively small R_{et} of Cu/TiO_2 can be affected by Cu_2O on its surface, probably behaving as a semiconductor to induce the electron transfer.[60] Based on the fitting analysis using the equivalent circuit model, the Au/TiO_2, $Au_{50}Cu_{50}/TiO_2$, and $Au_{20}Cu_{80}/TiO_2$ photocatalysts

https://doi.org/10.1021/acsomega.2c03509
ACS Omega 2022, 7, 31260−31270

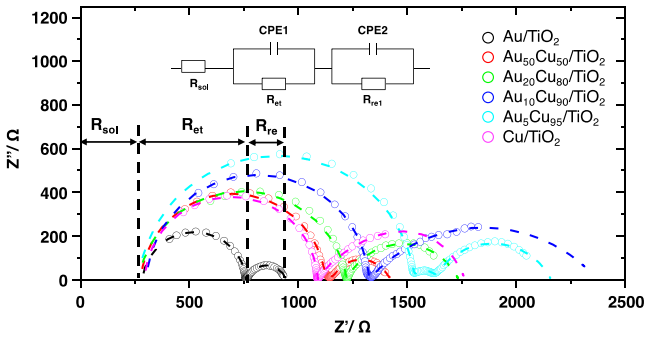

Figure 8. EIS Nyquist plots of Au−Cu/TiO_2 in formic acid solution (0.010 M) under light irradiation (15 mW cm^{-2}). The plots shown by circles are measured values, and the dotted lines are the spectra calculated from the fitting results.

show R_{re} values of 184, 345, and 513 Ω, respectively, that are smaller than $Au_{10}Cu_{90}/TiO_2$ (1051 Ω) and Au_5Cu_{95}/TiO_2 (628 Ω). An additional arc observed at the region of R_{re} for Au_5Cu_{95}/TiO_2 can be attributed to the Cu^+ leaching from Au_5Cu_{95} NPs. The results illustrate the tendency of Au to improve the electron transfer efficiency. Based on the EIS analysis, Au/TiO_2 is expected to show the highest H_2 evolution rates among Au−Cu/TiO_2 films; nevertheless, the observed H_2 evolution rates in Figure 6a are comparable when the Au content is up to 20%. This obviously suggests that the RDS in the H_2 evolution is neither the electron transfer nor formic acid decomposition. The EIS analysis is consistent with the KIE result that the reaction of a surface-active species with protons is involved in the RDS.

Based on the above results and a previous report,[61] a plausible mechanism for the H_2 evolution from formic acid dehydrogenation using the Au−Cu/TiO_2 photocatalysts is illustrated in Figure 8. The H_2 evolution from formic acid dehydrogenation using Au−Cu/TiO_2 photocatalysts is achieved through three essential steps (Figure 9a): (1) Upon light irradiation (λ = 365 nm), the electrons and holes are generated in TiO_2. (2) Subsequently, the holes of TiO_2 react with HCOOH to form CO_2 and protons. As the vibrational modes of HCOO molecules were observed in the Raman spectra of $Au_{20}Cu_{80}/TiO_2$ in Figure 7b, formic acid is likely oxidized by the holes. However, it cannot deny the possibility of oxidation by hydroxyl radicals. (3) The photogenerated electrons migrate from TiO_2 to the Au−Cu alloy NPs that function as an electron sink, and protons are reduced by a surface-reactive species,[62] leading to H_2 evolution. The RDS in the H_2 evolution is involved in the reaction of protons with the surface-active species based on the EIS and KIE analysis.

The catalytic activity of Au−Cu/TiO_2 was significantly changed between the Au contents of 20 and 10 at%. When the Au content was less than 20 at%, the surface of Au−Cu NPs was naturally oxidized and covered by Cu_2O layers (Figure 4f) and suffered from the considerable leaching of Cu atoms after the reactions (Figure S16). The Cu_2O layers on the surfaces of Au−Cu/TiO_2 can disturb the electron migration evidenced by the large R_{et} (Figure 8) and inhibit surface electron accumulation on AuCu NPs. It simultaneously accelerates the recombination of electrons and holes generated in TiO_2,[63] resulting in low H_2 evolution rates (Figure 9b). On the other hand, the relatively large Au content (Au ≥ 20 at%) in Au−Cu/TiO_2 preserves the Cu atoms from oxidation as well as it induces electron transfer efficiency, which is favorable for the H_2 evolution (Figure 9c). In addition, the H_2 evolution of Au−Cu/TiO_2 (Au ≥ 20 at%) photocatalysts exhibited comparable reactivities to pure Au/TiO_2 because the RDS is the reaction of a surface-active species with protons rather than the electron transfer.

CONCLUSIONS

Well-defined Au−Cu/TiO_2 photocatalyst films were successfully synthesized by depositing Au−Cu alloy NPs onto TiO_2 NP films via the laser ablation method along with the aerosol deposition technique. In formic acid dehydrogenation, the as-prepared Au−Cu/TiO_2 films exhibited high H_2 evolution rates under LED irradiation (λ = 365 nm). No H_2 evolution was observed in the dark condition, demonstrating the ability of Au−Cu/TiO_2 films for a switchable on-demand H_2 production. The $Au_{20}Cu_{80}/TiO_2$ photocatalyst film exhibited a high H_2 evolution rate comparable to pure Au/TiO_2 and significantly higher activity than Cu/TiO_2. The XPS analysis demonstrated that the Au−Cu nanoalloys with more than 20 at% Au maintained a metallic state and induced the interfacial electron transfers from TiO_2 to the Au−Cu alloy NPs, improving catalytic activity and stability. The KIE and EIS analysis confirmed that the RDS in the H_2 evolution is involved in the reaction of a surface-active species with protons. Efficient and recycled Au−Cu alloy NPs deposited on the TiO_2 photocatalyst with on/off switching ability showed great promise for an on-demand H_2 production in practical applications. Identifying suitable base metals and optimizing the nanoalloy composition using the gas-phase laser ablation method are highly effective strategies for the contaminant and surfactant-free synthesis of various nanoparticles for developing photocatalysts.

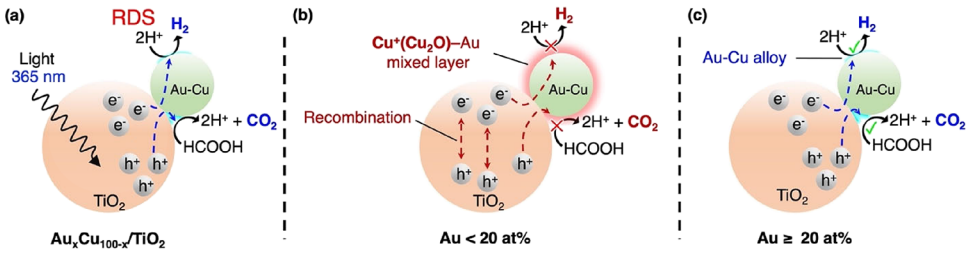

Figure 9. Schematic illustration of the proposed mechanism for the H_2 evolution from formic acid dehydrogenation by Au−Cu/TiO_2 photocatalysts.

https://doi.org/10.1021/acsomega.2c03509
ACS Omega 2022, 7, 31260−31270

■ ASSOCIATED CONTENT

Supporting Information

The Supporting Information is available free of charge at https://pubs.acs.org/doi/10.1021/acsomega.2c03509.

Photographs of Au−Cu/TiO_2 films (Figure S1), experimental setup (Figure S2), Au contents by XRD and ICP-MS (Table S1), TEM images (Figures S3 and S15), particle size distribution (Figure S4), diffuse reflectance UV−vis spectra (Figure S5), XPS spectra (Figures S6, S7, and S17), time courses of CO_2 and CO evolution (Figures S8, S9, S10, S12 and S13), activity comparison (Table S2), apparent quantum yield (Figure S11), long-term stability (Figure S14), Au contents by XPS (Figure S16), ohmic resistance (Table S3), and plots of resistances (Figure S18) (PDF)

■ AUTHOR INFORMATION

Corresponding Authors

Dachao Hong − *Interdisciplinary Research Center for Catalytic Chemistry, National Institute of Advanced Industrial Science and Technology, Tsukuba, Ibaraki 305-8565, Japan;* orcid.org/0000-0003-0581-1315; Email: hong-d@aist.go.jp

Kenji Koga − *Nanomaterials Research Institute, National Institute of Advanced Industrial Science and Technology, Tsukuba, Ibaraki 305-8565, Japan;* orcid.org/0000-0003-2546-5050; Email: k.koga@aist.go.jp

Authors

Aditya Sharma − *Interdisciplinary Research Center for Catalytic Chemistry, National Institute of Advanced Industrial Science and Technology, Tsukuba, Ibaraki 305-8565, Japan*

Dianping Jiang − *Nanomaterials Research Institute, National Institute of Advanced Industrial Science and Technology, Tsukuba, Ibaraki 305-8565, Japan*

Elena Stellino − *Physics and Geology Department, University of Perugia, 06123 Perugia, Italy;* orcid.org/0000-0001-6385-4589

Tomohiro Ishiyama − *Research Institute for Energy Conservation, National Institute of Advanced Industrial Science and Technology, Tsukuba, Ibaraki 305-8565, Japan;* orcid.org/0000-0003-0956-6740

Paolo Postorino − *Physics Department, Sapienza University of Rome, 00185 Rome, Italy;* orcid.org/0000-0002-3809-0676

Ernesto Placidi − *Physics Department, Sapienza University of Rome, 00185 Rome, Italy;* orcid.org/0000-0002-3820-8451

Yoshihiro Kon − *Interdisciplinary Research Center for Catalytic Chemistry, National Institute of Advanced Industrial Science and Technology, Tsukuba, Ibaraki 305-8565, Japan;* orcid.org/0000-0002-7217-0557

Complete contact information is available at: https://pubs.acs.org/10.1021/acsomega.2c03509

Notes

The authors declare no competing financial interest.

■ ACKNOWLEDGMENTS

This work was partially supported by Grants-in-Aid (no. 21K05104) from Japan Society for the Promotion of Science (JSPS). D.H. gratefully acknowledges support from JSPS by the Leading Initiative for Excellent Young Researchers (LEADER). E.P. and P.P. are grateful to the support of Sapienza Grande Progetto di Ateneo 2017, Amaldi Research Centre (MIUR program "Dipartimento di Eccellenza" CUP: B81I18001170001) and to Marco Sbroscia for the technical assistance in the experiments. The ICP−MS analysis was carried out through the Nanotechnology Network Project of the Ministry of Education, Culture, Sports, Science and Technology (MEXT), Japan. We want to acknowledge Masakazu Takata for assisting the research.

■ REFERENCES

(1) Zhong, H.; Iguchi, M.; Chatterjee, M.; Himeda, Y.; Xu, Q.; Kawanami, H.; Zhong, H.; Iguchi, M.; Chatterjee, M.; Kawanami, H.; Himeda, Y.; Xu, Q. Formic Acid-Based Liquid Organic Hydrogen Carrier System with Heterogeneous Catalysts. *Adv. Sustainable Syst.* **2018**, *2*, 1700161.

(2) Zhu, J.; Hu, L.; Zhao, P.; Lee, L. Y. S.; Wong, K. Y. Recent Advances in Electrocatalytic Hydrogen Evolution Using Nanoparticles. *Chem. Rev.* **2020**, *120*, 851−918.

(3) Matsumoto, K.; Onoda, A.; Campidell, S.; Hayashi, T. Electrocatalytic Hydrogen Evolution Reaction Promoted by Co/N/C Catalysts with CoNx Active Sites Derived from Precursors Forming N-Doped Graphene Nanoribbons. *Bull. Chem. Soc. Jpn.* **2021**, *94*, 2898−2905.

(4) Sakaushi, K. Science of Electrode Processes in the 21st Century: Fundamental Understanding of Microscopic Mechanisms towards Advancing Electrochemical Technologies. *Bull. Chem. Soc. Jpn.* **2021**, *94*, 2423−2434.

(5) Ren, Y.; Li, Z.; Deng, B.; Ye, C.; Zhang, L.; Wang, Y.; Li, T.; Liu, Q.; Cui, G.; Asiri, A. M.; et al. Superior Hydrogen Evolution Electrocatalysis Enabled by CoP Nanowire Array on Graphite Felt. *Int. J. Hydrogen Energy* **2022**, *47*, 3580−3586.

(6) Lewis, N. S.; Nocera, D. G. Powering the Planet: Chemical Challenges in Solar Energy Utilization. *Proc. Natl. Acad. Sci. U. S. A.* **2006**, *103*, 15729−15735.

(7) Fukuzumi, S. Bioinspired Energy Conversion Systems for Hydrogen Production and Storage. *Eur. J. Inorg. Chem.* **2008**, *2008*, 1351−1362.

(8) Moradi, R.; Groth, K. M. Hydrogen Storage and Delivery: Review of the State of the Art Technologies and Risk and Reliability Analysis. *Int. J. Hydrogen Energy* **2019**, *44*, 12254−12269.

(9) Fukuzumi, S.; Suenobu, T. Hydrogen Storage and Evolution Catalysed by Metal Hydride Complexes. *Dalton Trans.* **2013**, *42*, 18−28.

(10) Hong, D.; Shimoyama, Y.; Ohgomori, Y.; Kanega, R.; Kotani, H.; Ishizuka, T.; Kon, Y.; Himeda, Y.; Kojima, T. Cooperative Effects of Heterodinuclear IrIII−MII Complexes on Catalytic H2 Evolution from Formic Acid Dehydrogenation in Water. *Inorg. Chem.* **2020**, *59*, 11976−11985.

(11) Wang, W. H.; Ertem, M. Z.; Xu, S.; Onishi, N.; Manaka, Y.; Suna, Y.; Kambayashi, H.; Muckerman, J. T.; Fujita, E.; Himeda, Y. Highly Robust Hydrogen Generation by Bioinspired Ir Complexes for Dehydrogenation of Formic Acid in Water: Experimental and Theoretical Mechanistic Investigations at Different pH. *ACS Catal.* **2015**, *5*, 5496−5504.

(12) Navlani-García, M.; Mori, K.; Salinas-Torres, D.; Kuwahara, Y.; Yamashita, H. New Approaches toward the Hydrogen Production from Formic Acid Dehydrogenation over Pd-Based Heterogeneous Catalysts. *Front. Mater.* **2019**, *6*, 44.

(13) Zhong, S.; Yang, X.; Chen, L.; Tsumori, N.; Taguchi, N.; Xu, Q. Interfacing with Fe-N-C Sites Boosts the Formic Acid Dehydrogenation of Palladium Nanoparticles. *ACS Appl. Mater. Interfaces* **2021**, *13*, 46749−46755.

(14) Marcinkowski, M. D.; Liu, J.; Murphy, C. J.; Liriano, M. L.; Wasio, N. A.; Lucci, F. R.; Flytzani-Stephanopoulos, M.; Sykes, E. C.

H. Selective Formic Acid Dehydrogenation on Pt-Cu Single-Atom Alloys. *ACS Catal.* **2017**, *7*, 413−420.
(15) Kuehnel, M. F.; Wakerley, D. W.; Orchard, K. L.; Reisner, E. Photocatalytic Formic Acid Conversion on CdS Nanocrystals with Controllable Selectivity for H2 or CO. *Angew. Chem., Int. Ed.* **2015**, *54*, 9627−9631.
(16) Nasir, J. A.; Hafeez, M.; Arshad, M.; Ali, N. Z.; Teixeira, I. F.; McPherson, I.; Khan, M. A. Photocatalytic Dehydrogenation of Formic Acid on CdS Nanorods through Ni and Co Redox Mediation under Mild Conditions. *ChemSusChem* **2018**, *11*, 2587−2592.
(17) Tsuji, M.; Shimamoto, D.; Uto, K.; Hattori, M.; Ago, H. Enhancement of Catalytic Activity of AgPd@Pd/TiO2 Nanoparticles under UV and Visible Photoirradiation. *J. Mater. Chem. A* **2016**, *4*, 14649−14656.
(18) Yin, Y.; Yang, Y.; Zhang, L.; Li, Y.; Li, Z.; Lei, W.; Ma, Y.; Huang, Z. Facile Synthesis of Au/Pd Nano-Dogbones and Their Plasmon-Enhanced Visible-to-NIR Light Photocatalytic Performance. *RSC Adv.* **2017**, *7*, 36923−36928.
(19) Gazsi, A.; Schubert, G.; Pusztai, P.; Solymosi, F. Photocatalytic Decomposition of Formic Acid and Methyl Formate on TiO2 Doped with N and Promoted with Au. Production of H2. *Int. J. Hydrogen Energy* **2013**, *38*, 7756−7766.
(20) Caner, N.; Bulut, A.; Yurderi, M.; Ertas, I. E.; Kivrak, H.; Kaya, M.; Zahmakiran, M. Atomic Layer Deposition-SiO2 Layers Protected PdCoNi Nanoparticles Supported on TiO2 Nanopowders: Exceptionally Stable Nanocatalyst for the Dehydrogenation of Formic Acid. *Appl. Catal., B* **2017**, *210*, 470−483.
(21) Tong, F.; Lou, Z.; Liang, X.; Ma, F.; Chen, W.; Wang, Z.; Liu, Y.; Wang, P.; Cheng, H.; Dai, Y.; Zheng, Z.; Huang, B. Plasmon-Induced Dehydrogenation of Formic Acid on Pd-Dotted Ag@Au Hexagonal Nanoplates and Single-Particle Study. *Appl. Catal., B* **2020**, *277*, 119226.
(22) Zhang, S.; Duan, S.; Chen, G.; Meng, S.; Zheng, X.; Fan, Y.; Fu, X.; Chen, S. MoS2/Zn3In2S6 Composite Photocatalysts for Enhancement of Visible Light-Driven Hydrogen Production from Formic Acid. *Chin. J. Catal.* **2021**, *42*, 193−204.
(23) Wang, J.; Wang, X.; Qiu, L.; Wang, H.; Duan, L.; Kang, Z.; Liu, J. Photocatalytic Selective H2 Release from Formic Acid Enabled by CO_2 Captured Carbon Nitride. *Nanotechnology* **2021**, *32*, 275404.
(24) Gao, W.; Liu, Q.; Zhao, X.; Cui, C.; Zhang, S.; Zhou, W.; Wang, X.; Wang, S.; Liu, H.; Sang, Y. Electromagnetic Induction Effect Induced High-Efficiency Hot Charge Generation and Transfer in Pd-Tipped Au Nanorods to Boost Plasmon-Enhanced Formic Acid Dehydrogenation. *Nano Energy* **2021**, *80*, 105543.
(25) Ibrahim, N. S.; Leaw, W. L.; Mohamad, D.; Alias, S. H.; Nur, H. A Critical Review of Metal-Doped TiO2 and Its Structure−Physical Properties−Photocatalytic Activity Relationship in Hydrogen Production. *Int. J. Hydrogen Energy* **2020**, *45*, 28553−28565.
(26) Liang, Q.; Liu, X.; Zeng, G.; Liu, Z.; Tang, L.; Shao, B.; Zeng, Z.; Zhang, W.; Liu, Y.; Cheng, M.; Tang, W.; Gong, S. Surfactant-Assisted Synthesis of Photocatalysts: Mechanism, Synthesis, Recent Advances and Environmental Application. *Chem. Eng. J.* **2019**, *372*, 429−451.
(27) Lin, Z.; Shen, S.; Wang, Z.; Zhong, W. Laser Ablation in Air and Its Application in Catalytic Water Splitting and Li-Ion Battery. *iScience* **2021**, *24*, 102469.
(28) Jaleh, B.; Nasrollahzadeh, M.; Mohazzab, B. F.; Eslamipanah, M.; Sajjadi, M.; Ghafuri, H. State-of-the-Art Technology: Recent Investigations on Laser-Mediated Synthesis of Nanocomposites for Environmental Remediation. *Ceram. Int.* **2021**, *47*, 10389−10425.
(29) Kim, M.; Osone, S.; Kim, T.; Higashi, H.; Seto, T. Synthesis of Nanoparticles by Laser Ablation: A Review. *Kona Powder Part. J.* **2017**, *34*, 80−90.
(30) Ashfold, M. N. R.; Claeyssens, F.; Fuge, G. M.; Henley, S. J. Pulsed Laser Ablation and Deposition of Thin Films. *Chem. Soc. Rev.* **2004**, *33*, 23−31.
(31) Gu, X.; Lu, Z.-H.; Jiang, H.-L.; Akita, T.; Xu, Q. Synergistic Catalysis of Metal−Organic Framework-Immobilized Au−Pd Nanoparticles in Dehydrogenation of Formic Acid for Chemical Hydrogen Storage. *J. Am. Chem. Soc.* **2011**, *133*, 11822−11825.
(32) Koga, K.; Hirasawa, M. Anisotropic Growth of NiO Nanorods from Ni Nanoparticles by Rapid Thermal Oxidation. *Nanotechnology* **2013**, *24*, 375602.
(33) Koga, K.; Zubia, D. Strain Analysis of AuxCu1-X−Cu2O Biphase Nanoparticles with Heteroepitaxial Interface. *J. Phys. Chem. C* **2008**, *112*, 2079−2085.
(34) Koga, K.; Hirasawa, M. Gas-Phase Fabrication of Noble Metal-γ-Al2O3 Janus Nanoparticles and Nanoworms. *J. Mater. Sci.* **2016**, *51*, 3250−3256.
(35) Moulder, J.; Stickle, W.; Sobol, P.; Bomben, K. *Handbook of X-Ray Photoelectron Spectroscopy (XPS)*; Jill, C., Ed.; Perkin-Elmer Corporation: Minnesota, United States of America, 1992; Vol. 2.
(36) Shimoyama, Y.; Koga, K.; Tabe, H.; Yamada, Y.; Kon, Y.; Hong, D. RuO_2 Nanoparticle-Embedded Graphitic Carbon Nitride for Efficient Photocatalytic H2 Evolution. *ACS Appl. Nano Mater.* **2021**, *4*, 11700−11708.
(37) Hong, D.; Lyu, L. M.; Koga, K.; Shimoyama, Y.; Kon, Y. Plasmonic Ag@TiO2 Core-Shell Nanoparticles for Enhanced CO2 Photoconversion to CH4. *ACS Sustainable Chem. Eng.* **2019**, *7*, 18955−18964.
(38) Tan, T. H.; Scott, J. A.; Ng, Y. H.; Taylor, R. A.; Aguey-Zinsou, K. F.; Amal, R. Plasmon Enhanced Selective Electronic Pathways in TiO_2 Supported Atomically Ordered Bimetallic Au-Cu Alloys. *J. Catal.* **2017**, *352*, 638−648.
(39) Neaţu, S.; Maciá-Agulló, J. A.; Concepción, P.; Garcia, H. Gold-Copper Nanoalloys Supported on TiO_2 as Photocatalysts for CO_2 Reduction by Water. *J. Am. Chem. Soc.* **2014**, *136*, 15969−15976.
(40) Sandoval, A.; Louis, C.; Zanella, R. Improved Activity and Stability in CO Oxidation of Bimetallic Au-Cu/TiO2 Catalysts Prepared by Deposition-Precipitation with Urea. *Appl. Catal., B* **2013**, *140−141*, 363−377.
(41) Gonella, F.; Mattei, G.; Mazzoldi, P.; Sada, C.; Battaglin, G.; Cattaruzza, E. Au−Cu Alloy Nanoclusters in Silica Formed by Ion Implantation and Annealing in Reducing or Oxidizing Atmosphere. *Appl. Phys. Lett.* **1999**, *75*, 55.
(42) Majhi, J. K.; Kuiri, P. K. Large Spectral Shift of Plasmon Resonances in Au−Cu Alloy Nanoparticles through Anisotropy and Interaction. *Bull. Mater. Sci.* **2021**, *44*, 1−7.
(43) Chen, J.; Xiao, P.; Gu, J.; Huang, Y.; Zhang, J.; Wang, W.; Chen, T. Au Nanoparticle-Loaded PDMAEMA Brush Grafted Graphene Oxide Hybrid Systems for Thermally Smart Catalysis. *RSC Adv.* **2014**, *4*, 44480−44485.
(44) Yu, Y.; Dong, X.; Chen, P.; Geng, Q.; Wang, H.; Li, J.; Zhou, Y.; Dong, F. Synergistic Effect of Cu Single Atoms and Au-Cu Alloy Nanoparticles on TiO2 for Efficient CO2 Photoreduction. *ACS Nano* **2021**, *15*, 14453−14464.
(45) Kuhn, M.; Sham, T. K. Charge Redistribution and Electronic Behavior in a Series of Au-Cu Alloys. *Phys. Rev. B* **1994**, *49*, 1647−1661.
(46) Fernandez, V.; Kiani, D.; Fairley, N.; Felpin, F. X.; Baltrusaitis, J. Curve Fitting Complex X-Ray Photoelectron Spectra of Graphite-Supported Copper Nanoparticles Using Informed Line Shapes. *Appl. Surf. Sci.* **2020**, *505*, 143841.
(47) Casaletto, M. P.; Longo, A.; Martorana, A.; Prestianni, A.; Venezia, A. M. XPS Study of Supported Gold Catalysts: The Role of Au0 and Au+δ Species as Active Sites. *Surf. Interface Anal.* **2006**, *38*, 215−218.
(48) Sha, J.; Paul, S.; Dumeignil, F.; Wojcieszak, R. Au-Based Bimetallic Catalysts: How the Synergy between Two Metals Affects Their Catalytic Activity. *RSC Adv.* **2019**, *9*, 29888−29901.
(49) Klyushin, A. Y.; Greiner, M. T.; Huang, X.; Lunkenbein, T.; Li, X.; Timpe, O.; Friedrich, M.; Hävecker, M.; Knop-Gericke, A.; Schlögl, R. Is Nanostructuring Sufficient to Get Catalytically Active Au? *ACS Catal.* **2016**, *6*, 3372−3380.
(50) Chimentão, R. J.; Medina, F.; Fierro, J. L. G.; Llorca, J.; Sueiras, J. E.; Cesteros, Y.; Salagre, P. Propene Epoxidation by Nitrous Oxide

https://doi.org/10.1021/acsomega.2c03509
ACS Omega 2022, 7, 31260−31270

over Au−Cu/TiO2 Alloy Catalysts. *J. Mol. Catal. A: Chem.* **2007**, *274*, 159−168.
(51) Nugraha, A. S.; Malgras, V.; Iqbal, M.; Jiang, B.; Li, C.; Bando, Y.; Alshehri, A.; Kim, J.; Yamauchi, Y.; Asahi, T. Electrochemical Synthesis of Mesoporous Au-Cu Alloy Films with Vertically Oriented Mesochannels Using Block Copolymer Micelles. *ACS Appl. Mater. Interfaces* **2018**, *10*, 23783−23791.
(52) Wang, G.; Xiao, L.; Huang, B.; Ren, Z.; Tang, X.; Zhuang, L.; Lu, J. AuCu Intermetallic Nanoparticles: Surfactant-Free Synthesis and Novel Electrochemistry. *J. Mater. Chem.* **2012**, *22*, 15769−15774.
(53) Biesinger, M. C. Advanced Analysis of Copper X-Ray Photoelectron Spectra. *Surf. Interface Anal.* **2017**, *49*, 1325−1334.
(54) Liu, M.; Zhou, W.; Wang, T.; Wang, D.; Liu, L.; Ye, J. High Performance Au−Cu Alloy for Enhanced Visible-Light Water Splitting Driven by Coinage Metals. *Chem. Commun.* **2016**, *52*, 4694−4697.
(55) Cao, S.; Chen, Y.; Wang, H.; Chen, J.; Shi, X.; Li, H.; Cheng, P.; Liu, X.; Liu, M.; Piao, L. Ultrasmall CoP Nanoparticles as Efficient Cocatalysts for Photocatalytic Formic Acid Dehydrogenation. *Joule* **2018**, *2*, 549−557.
(56) Nouruzi, N.; Dinari, M.; Gholipour, B.; Mokhtari, N.; Farajzadeh, M.; Rostamnia, S.; Shokouhimehr, M. Photocatalytic Hydrogen Generation Using Colloidal Covalent Organic Polymers Decorated Bimetallic Au-Pd Nanoalloy (COPs/Pd-Au). *Mol. Catal.* **2022**, *518*, 112058.
(57) Luo, Y.; Yang, Q.; Nie, W.; Yao, Q.; Zhang, Z.; Lu, Z. H. Anchoring IrPdAu Nanoparticles on NH2-SBA-15 for Fast Hydrogen Production from Formic Acid at Room Temperature. *ACS Appl. Mater. Interfaces* **2020**, *12*, 8082−8090.
(58) Grasemann, M.; Laurenczy, G. Formic Acid as a Hydrogen Source − Recent Developments and Future Trends. *Energy Environ. Sci.* **2012**, *5*, 8171−8181.
(59) Paschoal, C. W. A.; Moura, M. R.; Ayala, A. P.; Sasaki, J. M.; Freire, P. T. C.; Melo, F. E. A.; Mendes Filho, J.; Guedes, I.; Leyva, A. G.; Polla, G.; Vega, D.; Perazzo, P. K. Temperature-Dependent Raman Study of $CaCu(HCOO)_4$ and $Ca_2Cu(HCOO)_6$ *Crystals. J. Solid State Chem.* **2000**, *154*, 338−343.
(60) Shao, Z.; Zhang, Y.; Yang, X.; Zhong, M. Au-Mediated Charge Transfer Process of Ternary Cu2O/Au/TiO2-NAs Nanoheterostructures for Improved Photoelectrochemical Performance. *ACS Omega* **2020**, *5*, 7503−7518.
(61) Kumaravel, V.; Mathew, S.; Bartlett, J.; Pillai, S. C. Photocatalytic Hydrogen Production Using Metal Doped TiO2: A Review of Recent Advances. *Appl. Catal., B* **2019**, *244*, 1021−1064.
(62) Liu, Y.; Xu, C.; Xie, Y.; Yang, L.; Ling, Y.; Chen, L. Au−Cu Nanoalloy/TiO2/MoS2 Ternary Hybrid with Enhanced Photocatalytic Hydrogen Production. *J. Alloys Compd.* **2020**, *820*, 153440.
(63) Wu, Y.; Lu, G.; Li, S. The Role of Cu(I) Species for Photocatalytic Hydrogen Generation over CuOx/TiO2. *Catal. Lett.* **2009**, *133*, 97−105.

https://doi.org/10.1021/acsomega.2c03509
ACS Omega 2022, 7, 31260−31270